HHS Public Access

Author manuscript

MAGMA. Author manuscript; available in PMC 2017 June 01.

Published in final edited form as:

MAGMA. 2016 June ; 29(3): 319–332. doi:10.1007/s10334-015-0515-2.

Correction of B_0-induced geometric distortion variations in prospective motion correction for 7T MRI

Uten Yarach[1,2], **Chaiya Luengviriya**[3], **Daniel Stucht**[1], **Frank Godenschweger**[1], **Peter Schulze**[1,5], and **Oliver Speck**[1,4,5,6]

[1] Department of Biomedical Magnetic Resonance, Otto-von-Guericke University Magdeburg, Leipziger Str. 44 (Haus 65), 39120 Magdeburg, Germany [2] Department of Radiological Technology, Chiangmai University, Chiang Mai, Thailand [3] Department of Physics, Kasetsart University, Bangkok, Thailand [4] Leibniz Institute for Neurobiology, Magdeburg, Germany [5] German Centre for Neurodegenerative Diseases (DZNE), Site Magdeburg, Magdeburg, Germany [6] Center for Behavioral Brain Sciences, Magdeburg, Germany

Abstract

Objective—Prospective motion correction can effectively fix the imaging volume of interest. For large motion, this can lead to relative motion of coil sensitivities, distortions associated with imaging gradients and B_0 field variations. This work accounts for the B_0 field change due to subject movement, and proposes a method for correcting tissue magnetic susceptibility-related distortion in prospective motion correction.

Materials and methods—The B_0 field shifts at the different head orientations were characterized. A volunteer performed large motion with prospective motion correction enabled. The acquired data were divided into multiple groups according to the object positions. The correction of B_0-related distortion was applied to each group of data individually via augmented sensitivity encoding with additionally integrated gradient nonlinearity correction.

Results—The relative motion of the gradients, B_0 field and coil sensitivities in prospective motion correction results in residual spatial distortion, blurring, and coil artifacts. These errors can be mitigated by the proposed method. Moreover, iterative conjugate gradient optimization with regularization provided superior results with smaller RMSE in comparison to standard conjugate gradient.

Conclusion—The combined correction of B_0-related distortion and gradient nonlinearity leads to a reduction of residual motion artifacts in prospective motion correction data.

Uten Yarach uten.yarach@st.ovgu.de.

Compliance with ethical standards

Conflict of interest The authors have no conflict of interest.

Ethical standard The measurements on human subjects in this study have been approved by the local ethics committee and have therefore been performed in accordance with the ethical standards laid down in the Declaration of Helsinki. All involved subjects have given their informed consent before recruitment in the study.

Keywords

Prospective motion correction; Gradient nonlinearity; B_0 field variations; Coil sensitivity; Augmented SENSE

Introduction

Artifacts caused by head movement during magnetic resonance imaging (MRI) can be corrected through retrospective [1–3] or prospective approaches [4–6]. Prospective motion correction (PMC) methods which adjust the imaging gradients and radiofrequency immediately before each excitation are receiving increasing attention due to the fact that they can prevent *k*-space inconsistencies and spin history effects. Furthermore, no extra imaging time is required when an external tracking system which commonly computes pose (position and orientation) in 6° of freedom is used [6].

Even with highly accurate and precise tracking and low-latency PMC, large scale motion can lead to residual artifacts [7] that cannot be compensated for with rigid body adjustment alone. Apart from the inherent tracking problem [8], the commonly discussed artifact sources are the relative motion of the coil sensitivities [9–13] and the gradient nonlinearity (GNL) [14–16]. Coil sensitivity misalignment due to physiological movement will cause variation of signal intensity and phase and lead to images with shading artifacts after root-sum-of-squares (RSS) combination of single coil images [9, 10]. This artifact appears more visible in parallel imaging with high acceleration factors [11] and also becomes more challenging with a large number of small array coils [12]. However, when the coil sensitivities relative to the object pose are given, this error can be corrected retrospectively as introduced by Bammer et al. [13], termed augmented sensitivity encoding (augmented SENSE) reconstruction. In addition, motion within a non-linear gradient manifests as spatial distortion and blurring since object geometry at multiple object poses within the non-linear gradient fields and thus the *k*-space data become inconsistent between phase encoding steps as demonstrated by Polzin et al. [14] and other authors [15]. This effect is more pronounced in peripheral regions where gradient deviations are strongest. Recently, we proposed a method to mitigate this *GNL*-related artifact by integrating a conventional *GNL* correction of partial *k*-space data into augmented SENSE [16]. In general, not only *GNL* can result in spatial distortion due to motion but B_0 inhomogeneity (ΔB_0) caused by magnetic properties of the subject (e.g., air-tissue interfaces) is a relevant source of geometric distortions [17–19]. Particularly, the geometric distortion is increased at high field strength such as 7T [20]. Recently, the locations and sizes of B_0 field shifts within the brain at 7T for different head movements were reported [21]. These observations showed that the local field changes strongly depend on the subject orientation. Consequently, PMC at high field may be impacted by this variation even in conventional sequences (i.e., Spin-Echo and Gradient-Echo) with low readout-bandwidth (BW) that are often chosen to optimize signal-to-noise (SNR) or contrast-to-noise (CNR) ratios in structural imaging.

In this study, we investigated B_0 field variations during motion and proposed a reconstruction scheme to mitigate ΔB_0-induced geometric distortion in PMC, termed the

augmented CG-SENSE with integrated ΔB_0&*GNL* corrections. Moreover, NUFFT-based gridding [22] was employed instead of conventional interpolation during the warping procedure (ΔB_0 and *GNL* corrections) in order to preserve high spatial frequency components including boundaries and small structures [23]. The effectiveness of the proposed iterative method with respect to residual artifacts was evaluated through numerical simulations as well as phantom studies. Finally the proposed method was applied to human brain MRI.

Theory

The relationship between MR measurement data m and the image v can be described as

$$m = \boldsymbol{E} \cdot v = \mathbf{FT} \cdot v \quad (1)$$

where $\boldsymbol{E}$ is the so-called forward or encoding operator. In Cartesian-sampled MRI with linear gradient fields and one homogeneous receiver coil, this operator only consists of a discrete Fourier transformation (DFT, **FT**).

The encoding operator of retrospective motion correction

Recently, the operator $\boldsymbol{E}$ describing the rigid motion within multiple receiver coils assuming perfectly linear gradients and homogeneous B_0 was introduced by Bammer et al. [13].

$$\boldsymbol{E} = \boldsymbol{G}_{\mathrm{F\_}\,kspace} \cdot \mathbf{\Lambda} \cdot \mathbf{FT} \cdot \mathbf{diag}\left\{\Omega_{\mathbf{inv}}\mathbf{c^j}\right\} \quad (2)$$

where c^j is the static coil sensitivity of channel *j*. Motion of the object is described by a matrix $\boldsymbol{\Omega}$ and its inversion $\boldsymbol{\Omega}_{\mathrm{inv}}$, whereas $\boldsymbol{\Lambda}$ is the corresponding transformation rule to $\boldsymbol{\Omega}$ in *k*-space. $\boldsymbol{G}_{\mathbf{F\_}k\mathbf{space}}$ represents the forward resampling operator transferring the *k*-space data from a regular Cartesian grid to the original sampling location corrupted by motion $\boldsymbol{\Lambda}$.

The encoding operator of PMC for Cartesian sampled MRI

With highly accurate PMC, the object motion $\boldsymbol{\Omega}$ can be fully compensated by the gradient rotation matrix $\boldsymbol{\Omega}_{\mathrm{PMC}}$ determined by the tracking system consisting of six parameters of rigid body motion (i.e., $\boldsymbol{\Omega} \cdot \boldsymbol{\Omega}_{\mathrm{PMC}} = \boldsymbol{\Lambda} \cdot \boldsymbol{\Lambda}_{\mathrm{PMC}} = \mathbf{Id}$, **Id**: identity matrix). This means that the PMC can maintain *k*-space consistency during the data acquisition. Thus, *k*-space gridding ($\boldsymbol{G}_{\mathrm{F\_}k\mathrm{space}} \cdot \boldsymbol{\Lambda}$) is no longer needed, leading to a simple operator $\boldsymbol{E}$ of pose *i* and channel *j*,

$$\boldsymbol{E}^{i,j} = \boldsymbol{M}^i \cdot \mathbf{FT} \cdot \boldsymbol{C}^{i,j} \quad (3)$$

For simplicity, the coil sensitivity of channel *j* specific to object pose *i*($\boldsymbol{C}^{i,j}$) was used here instead of diag $\{\boldsymbol{\Omega}_{\mathrm{inv}}{}^{Cj}\}$. $\boldsymbol{M}^i$ is a Cartesian sampling mask (1 = sampled, 0 = otherwise). When considering the effects of magnetic field-induced geometric distortion that change relative to the object (ΔB_0) and scanner location (*GNL*) for Cartesian sampled MRI, the distortion correction is commonly considered in the spatial domain using the pixel shift

method [17] that requires the undistorted field displacements. Therefore, the operator $\boldsymbol{E}$ can be simplified to

$$\boldsymbol{E}^{i,j}=\boldsymbol{M}^{i}\cdot\mathbf{FT}\cdot\boldsymbol{G}^{i}_{F\_image}\cdot\boldsymbol{\Psi}^{i}\cdot\boldsymbol{C}^{i,j} \quad (4)$$

where $\boldsymbol{\Psi}^{i}$ is a spatial warping operator caused by ΔB_0 and *GNL* at pose *i*. $\boldsymbol{G}_{\mathrm{F\_image}}$ is a forward resampling operator transferring the image data from a regular coordinate system to the warped coordinate system.

The 3D spatial warping operator $\boldsymbol{\Psi}^{i}$

More explicitly, the operator $\boldsymbol{\Psi}^{i}$ consists of a set of rigid ($\boldsymbol{\Omega}^{i}_{PMC}$) as well as non-rigid ($\boldsymbol{D}_0$, $\boldsymbol{D}_x$, $\boldsymbol{D}_y$, and $\boldsymbol{D}_z$) operators that act on the undistorted xyz coordinate as

$$\begin{aligned}
&\left[x_i^{'},y_i^{'},z_i^{'}\right]^{T}=\boldsymbol{\Psi}^{i}[x,y,z]^{T}\\
&[x_i,y_i,z_i]^{T}=\boldsymbol{\Omega}^{i}_{PMC}[x,y,z]^{T}\\
&x_i^{'}=x+\boldsymbol{D}_x(x_i,y_i,z_i)+\boldsymbol{D}_0(x_i,y_i,z_i)\\
&y_i^{'}=y+\boldsymbol{D}_y(x_i,y_i,z_i)\\
&z_i^{'}=z+\boldsymbol{D}_z(x_i,y_i,z_i)
\end{aligned} \quad (5)$$

where $\boldsymbol{D}_0$ is the B_0—related displacement, and $\boldsymbol{D}_x$, $\boldsymbol{D}_y$, $\boldsymbol{D}_z$ are the gradient nonlinearities in each of the three directions. They are functions of the coordinates at any pose *i*. Note that for non-EPI sequences, the bandwidth in phase encoding direction is infinite. Therefore, B_0-related distortions need only be considered along the single frequency encoding direction. For example, if the read encoding gradient is aligned with the x axis, phase encoding is performed along the *y* and *z* axes for a 3D MRI (Eq. 5).

The image reconstruction

The desired image *v* corresponding to the encoding operator in Eq. 4 was estimated via a linear least-square approach that minimizes the squared Euclidean norm of the residual (Eq. 6) using the conjugate gradient (CG) method [24].

$$\min_{v}\left\{\sum_{i,j}\left\|m^{i,j}-\boldsymbol{E}^{i,j}v\right\|_2^2\right\} \quad (6)$$

However, the CG may exhibit unstable convergence behavior. This is because the encoding matrix seems seriously ill-conditioned due to the large dimension and the mixed encoding scheme [25]. Furthermore, the measured data may be also corrupted by noise. To overcome this difficulty, 12-regularization was also incorporated,

$$\min_{v}\left\{\sum_{i,j}\left\|m^{i,j}-\boldsymbol{E}^{i,j}v_2^2\right\|+\|\lambda\boldsymbol{L}v\|_2^2\right\} \quad (7)$$

The regularization parameter λ (lambda) is a positive real constant, and $\boldsymbol{L}$ is here a tridiagonal (1 –2 1) matrix [26].

The algorithm

Prior iteration, the intermediate image a is estimated by summing all products of multiplication between the matrix $\boldsymbol{E}^{(i,j)H}$ and the measured data vector $m^{i,j}$. $\boldsymbol{E}^{(i,j)H}$ is termed decoding or reconstruction operator. It consists of inverse FFT (**iFT**), inverse resampling operator ($\boldsymbol{G}^{i}_{\text{I\_ image}}$) transferring the distorted image to the undistorted coordinate ($\boldsymbol{\Psi}^{i*}$), and the complex conjugate of the coil sensitivity ($\boldsymbol{C}^{(i,j)*}$).

$$a=\sum_{i,j}\boldsymbol{E}^{(i,j)H}\cdot m^{i,j}=\sum_{i,j}\boldsymbol{C}^{(i,j)*}\cdot\left(\boldsymbol{J}^{i}_{\Psi}\right)\cdot\boldsymbol{\Psi}^{i*}\cdot\boldsymbol{G}^{i}_{\text{I\_ image}}\cdot\mathbf{iFT}\cdot m^{i,j},\quad i=1,\ldots N,\quad j=1,\ldots,N_{\text{C}} \quad (8)$$

Note that the Jacobian-based intensity correction ($\boldsymbol{J}^{i}_{\Psi}$) is generally accounted when the approximated solution a is obtained by the standard distortion correction [17, 40]. However, it is not an explicit part of this reconstruction, as its effect is implicitly contained in the forward NUFFT operator as derived by Knoll et al. [27]. It also becomes a simple and effective preconditioned matrix for CG method [23]. N is the total pose number, and N_{C} is the total channel number.

During iteration, the proposed reconstruction algorithm consists of four steps in each iteration: data encoding, data decoding, channel and pose combination, and the CG unit. Given the vector residuum $p^{(n)}$($p^{(0)}$ = a) from the previous iteration n, the current iteration of number n + 1 is carried out as follows.

Step 1 data encoding of pose i, channel j:

$$d^{i,j}=\boldsymbol{E}^{(i,j)}p^{(n)}=\boldsymbol{M}^{i}\cdot\mathbf{FT}\cdot\boldsymbol{G}^{i}_{\text{F\_ image}}\cdot\boldsymbol{\Psi}^{i}\cdot\boldsymbol{C}^{i,j}p^{(n)} \quad (9)$$

The previous $p^{(n)}$ is encoded by $\boldsymbol{E}^{(i,j)}$ to get the partial k-space data of each pose and channel $d^{i,j}$. This step consists of coil-wise multiplication by coil sensitivity, followed by resampling along the spatially warped coordinate, transformed to k-space by FFT, and then multiplied by the sampling mask. The sampling mask keeps only acquired k-space lines, the rest are set to zeros.

Step 2 data decoding of pose i, channel j:

$$h^{i,j}=\boldsymbol{E}^{(i,j)H}d^{(i,j)}=\boldsymbol{C}^{i,j*}\cdot\boldsymbol{\Psi}^{i*}\cdot\boldsymbol{G}^{i}_{\mathrm{I}\_\,image}\cdot\mathbf{iFT}\cdot d^{i,j} \quad (10)$$

The partial *k*-space data $d^{i,j}$ are reconstructed by $\boldsymbol{E}^{(i,j)H}$, obtaining the partial image of each pose and channel $h^{i,j}$. This step performs inverse FFT, then channel-wise resampling along the spatially unwarped coordinate, followed by individual weighting by complex conjugate of coil sensitivity.

Step 3 channel and pose combination:

$$I_{comb}=\sum_{i}^{N}\left\{\sum_{j=1}^{N_c}h^{i,j}\right\} \quad (11)$$

The partial complex image $h^{i,j}$ of different channels and poses are combined.

Step 4 the CG unit:

Finally, the combined image I_{comb} is fed back into the CG unit. The residuum after CG is then used as the initialization for the next iteration. Note that the CG algorithm can be found in appendix C of Ref. [24].

A schematic diagram of the proposed algorithm is shown in Fig. 1. The four steps above are repeated until the maximum iteration number or the stopping criteria [24] are reached.

Materials and methods

Numerical simulations

The performance of the proposed method was first tested in numerical simulations using a Shepp–Logan phantom assuming a 2D axial image (FOV = 256 mm^2, pixel size = 1 mm^2). The intensity values in a circular region with diameter 32 mm within the upper circular part of this phantom were replaced by zeros to represent an air inclusion (Fig. 2a). The data encoding in Eq. 9 was applied to this modified phantom in order to generate the motion-corrupted MR signal of each pose and channel $d^{i,j}$. The $\boldsymbol{C}^{i,j}$ was simulated using Biot–Savart's law [28]. The *GNL* at the different poses was expanded using spherical harmonics information specific for the gradient system of the 7T scanner used in the experimental studies. The object-specific field maps (in Hz) at air/water interfaces were analytically calculated using Eq. 26 and 27 in Ref. [29]. These fields were divided by readout-bandwidth (assumed 200 Hz/pixel along the x-direction), obtaining the displacements in units of pixel. N = 8 (32 *k*-space lines along phase direction per any pose i) and N_c = 8 were assumed for this simulation. Identical information as used in artifact generation was applied in the correction process. The pattern of 2D motion with maximum 30° around *z*-axis is shown in Fig. 2c.

Phantom and in vivo experiments

All experiments were performed on an ultra-high field whole-body 7T MRI scanner (Siemens Healthcare, Erlangen, Germany) equipped with a 70 mT/m whole body gradient system (SC72). PMC was performed with a tracking system consisting of a single camera mounted inside the scanner bore and a tracking marker with a multilayer structure, which generates moiré patterns for accurate orientation measurement [30]. Communication with the tracking system was implemented directly on the real-time control unit of the scanner as previously described by Zaitsev et al. [6].

Phantom experiments

An 18 cm diameter homemade phantom with a central air inclusion (ping pong ball) and further small structures was built. This phantom was filled with silicone oil, whose dielectric properties result in minor RF-excitation inhomogeneity only [31]. The phantom was scanned at two different constant poses with PMC enabled. In the second pose, the phantom was rotated ~33° around the *y*-axis. An 8-channel head coil (Rapid Biomedical, Rimpar, Germany) was used. Each constant pose was scanned at two different echo times (TE). Both TE's data were used to estimate the B_0 field map (ΔB_0) for each pose. The acquisition parameters were 3D FLASH with matrix: 192 × 192 × 144, voxel size: 1 × 1 × 1.3 mm, TR/TE1/TE2: 6.00/2.55/3.06 ms, and BW = 250 Hz/pixel. The synthetic corrupted data were created by combining the raw data of the two poses, assuming 2, 3, 4, 6, and 12 motions (i.e., 96, 64, 48, 32, and 16 *k*-space lines along phase direction per pose).

In vivo experiments

Two studies were carried out with one healthy male volunteer after informed consent according to the IRB-approved protocol. All data were acquired with PMC enabled using a 32-channel head coil (Nova Medical, Wilmington, MA, USA). The marker was securely attached to a mouth guard which was individually molded to the volunteer's upper teeth using a medical grade hydroplastic.

1. The characterization of size and location of B_0 field shifts within the brain at the different head orientations was performed using dual TE 3D FLASH with matrix; 256 × 256 × 176, voxel size; 1 × 1 × 1 mm, TR/TE1/TE2; 10.00/3.06/5.84 ms, and BW; 250 Hz/pixel. The volunteer was imaged at five orientations produced by roll rotation (around *z*-axis of the scanner). The volunteer was instructed to move the head between poses but otherwise remain still.

2. The application of the proposed method to real motion with PMC enabled was performed using 3D MPRAGE with the same resolution as 3D FLASH, TR/TE/TI; 1800/1.99/1050 ms, and BW; 200 Hz/pixel. After the first half of the acquisition, the volunteer was instructed to perform a one-time head rotation around the z-axis. The motion pattern from the tracking log file is shown in Fig. 7d. The field maps were also measured before and after motion and incorporated into the proposed reconstruction.

Data processing

The reconstruction was performed using MATLAB (version 12, The MathWorks Inc.), running on a Linux system. The voxel shift maps (VSM, $\boldsymbol{D}_0$ in Eq. 5) were generated as follows. First, the phase differences were calculated via the sum over channels of the Hermitian inner product using Eq. 3 in Ref. [32]. Second, the phase differences were unwrapped using FSL-PRELUDE and multiplied by FSL-BET's binary mask [33]. The unwrapped phases were divided by $2\pi(\Delta TE)$ to yield the field maps in units of Hz, followed by a 3 × 3 × 3 median filter to reduce noise. Finally, the field map was converted to the VSM using Eqs. 7–9 in Ref. [34]. The forward ($\boldsymbol{G}_F$) and the inverse ($\boldsymbol{G}_I$) resampling operators using min–max interpolation on a denser grid (2× oversampling) were calculated using Fessler's NUFFT package [28]. The coil sensitivities ($C^{i,j}$) were estimated from the central 64 × 64 × 64 *k*-space data of 3D FLASH specific to motion pose. These data were truncated by a cosine tapper window, and then transformed to images by FFT. Each individual-channel image was divided by the RSS image. The performance of the methods were evaluated by calculation of the root mean square error (RMSE), which was computed as

$$RMSE=\sqrt{\frac{\sum_{k=1}^{n}[im\,(k)-ref\,(k)]^2}{n}} \quad (12)$$

where ref is the reference image and im is the reconstructed image, n denotes the total number of pixels.

Results

Simulation results

Figure 2b shows that the RSS combination yielded images with severe artifacts caused by ΔB_0, *GNL*, and coil sensitivities misalignment. After applying augmented CG-SENSE the residual geometric distortions and field artifacts remain (Fig. 2d) particularly in the regions where the field effects are strongest as pointed out by the white (*GNL*'s effect) and yellow arrow (ΔB_0's effect) in the subtraction image (Fig. 2e). Integrating the *GNL* corrections into the reconstruction, the strong distortion around the periphery can be effectively reduced (Fig. 2f). The RMSE is reduced from 0.24 to 0.06 (Fig. 2g). Further improvement can be achieved when taking both ΔB_0 and *GNL* corrections into account (Fig. 2h). Note that the regularization technique was not applied to this simulation, since we found that the outcome did not depend on regularization. This is likely due to the absence of noise. The very small residual difference (Fig. 2i) may be due to imperfection in the interpolation. The pixel values at transformed coordinates are only an approximation by considering a few closely neighboring known pixels. Consequently, the image will lose quality with each iteration, in particular in regions of strong distortion.

Phantom results

Figure 3a demonstrates the gradient displacements and B_0 inhomogeneity associated with two object positions. The susceptibility induced field inhomogeneities at air/oil boundaries were up to 670 Hz. It is obvious and expected that their orientations strongly depend on the

object pose. The upper row of Fig. 3b shows two individual distorted images reconstructed by the RSS method. The GNL and ΔB_0 resulted in strong shape differences as pointed out by white arrows (GNL's effect) and black arrows (ΔB_0's effect) in the subtraction image. The bottom row of Fig. 3b shows that after GNL and ΔB_0 corrections, their shapes appear highly similar to each other, i.e., the subtraction image showed very small differences, demonstrating the correct estimation of GNL and ΔB_0 in this static situation. Inhomogeneity-induced signal loss due to intra-voxel dephasing was still present and is likely the main cause of the residual differences.

Figure 4a shows all variants of these combined data reconstructed by the different reconstruction schemes. The RSS method yielded images with severe artifacts caused by GNL, ΔB_0, and coil sensitivities misalignment (1st column). Although, augmented CG-SENSE largely reduced the sensitivity maps artifact, the spatial distortions and the blurring at the periphery and air/oil boundaries remain clearly visible (2nd column). These regions further improved when both GNL and ΔB_0 were addressed in augmented SENSE (4th column). Furthermore, high intensity variations near air/oil boundaries were remarkably reduced when using the regularization technique (3rd and 5th columns). Figure 4a also shows that the proposed method still worked well even when the synthetic motion trajectory switched rapidly back and forth between the two poses. The regularization also stabilized the solution, i.e., RMSEs at high iteration counts remain constant in contrast to conventional CG where RMSEs increase (4b).

In vivo results

Figure 5a, c show examples of B_0 field maps at identical slice positions relative to the subject's head from the volunteer scanned at five poses with prospectively corrected image orientation. The B_0 field variations at the frontal lobes (Fig. 2a) and the temporal lobe (Fig. 2c) were up to 650 and 400 Hz, respectively. Their amplitude and orientation changes relative to pose1 (0°) are shown in Fig. 5b, d as field differences. The motion induced field differences in the above mentioned regions were up to 250 and 150 Hz, respectively. This maximum observable B_0 shift (250 Hz) can cause 2.50 and 1.25 pixel shifts for the typical bandwidth of 100 and 200 Hz/pixel, respectively.

Figure 6a illustrates the B_0 field maps calculated from the full k-space, and the central k-space data with zero padding. The field map obtained from the central 32 × 32 × 32 k-space data appears largely different from the reference as shown in the field differences (Fig. 6b). We found that the central 64 × 64 × 64 k-space data still provided the proper field map with small field differences (Fig. 6b). In this study, these low resolution (low-res) field maps were chosen for the reconstruction in order to demonstrate that the reconstruction can be accomplished with low-res field map. Applying fast imaging sequences [35] to acquire the low-res field maps per motion pose may be possible.

Figure 7d shows the motion pattern when the subject performed the head rotation during the data acquisition. A maximum rotation around the z-axis of approx. 23° was detected. The motion data reconstructed by RSS (1st column) show blurring near the strong field B_0 field inhomogeneity and gradient field nonlinearity as pointed by yellow arrow (Fig. 7a1) and white arrow (Fig. 7a2), respectively. Moreover, noise and blurring artifacts are obviously

seen everywhere in Fig. 7a3. When the motion data was divided into two groups according to the tracking information, and then reconstructed by the augmented CG-SENSE with integrated *GNL* correction the peripheries appear much sharper (e.g., white arrow in Fig. 7b2). However, the blurring generated by ΔB_0 as pointed by yellow arrow (Fig. 7b1) still remains. Finally, the augmented CG-SENSE with integrated ΔB_0&*GNL* corrections can further improve the reconstructed image leading to a notable reduction of the above-mentioned artifacts (3rd column). It is obvious that the blurring artifact in the yellow circle regions (Fig. 7c3) appears much less visible when comparing with the same region of *GNL* corrected image (Fig. 7b3).

Figure 8 demonstrates the effectiveness of the proposed method for undersampled acquisition. The full *k*-space data were artificially accelerated by factor 2 × 2 along both phase directions (phase and slice directions). Although, the conventional CG-SENSE [24] provided the acceptable images (1st column), the remaining aliasing artifacts due to coil sensitivity misalignment and also the blurring artifacts caused by ΔB_0 and *GNL* are clearly visible as shown in the red circles. Note that sensitivity maps specific to the pose during the first half of the acquisition were used in conventional CG-SENSE. Superior image quality with very little remaining artifacts was achieved after applying the augmented CG-SENSE with integrated ΔB_0&*GNL* corrections (2nd column). Note that the regularized images in Figs. 4, 7, and 8 were reconstructed with the proper λ, which were manually selected. The values of 0.08–0.12 and 0.05 were used in phantom and in vivo experiments, respectively. Basically, using large λ results in slow convergence smooth result. In contrast, small λ converges rapidly, but returns more noisy results.

Discussion

Since MRI reconstruction relies on knowledge about the precise magnetic field at any position to create a map of proton density, any deviation from the assumed linear encoding field due to hardware-related sources (i.e., *GNL* and static B_0 field inhomogeneity) as well as subject-related sources (i.e., tissue-dependent chemical shift and susceptibility differences) can lead to small but relevant shifts in the apparent location of imaged structures in a stationary object [36, 37]. When the object is moving between acquisition steps, the amount and direction of local shift can change relative to the object. For small involuntary movement (<5°), the small local field shifts (±20 Hz) can degrade the image stability and decrease the *Z*-scores in a BOLD fMRI measurement [19]. In uncooperative patients who are unable to remain stationary larger motion may occur. Previous studies [7, 18, 21] showed that the local field shift increased proportionally to the amplitude of motion. Consequently, this can also slightly impact conventional Cartesian-sampled MRI as demonstrated in this study.

The geometric distortion caused by susceptibility differences is more complex due to the field inhomogeneity's dependency on the material (e.g., tissue, bone, and air), shape of the object, and its orientation relative to the static B_0 field. Recently, the size and location of B_0 field shifts within the brain at 7T for different types of head movement were studied by Sulikowska et al. [21]. Their results showed that the maximum B_0 field changes at the frontal lobe for pitch and yaw rotations were 4 ± 2 and 8 ± 11 Hz/degree, respectively. Other

authors have reported maximum B_0 field differences caused by head movement of 160 Hz at 2.89T [7] and 50 Hz at 3T [18]. In the present study, however, the field shifts are larger than reported in these previous studies. The motion induced field differences in the temporal and the frontal lobe were up to 150 and 250 Hz, respectively. This may be because the scale of motion in our study is large with rotations up to 25°. In addition, the field maps were acquired with very high spatial resolution and therefore localized field variations were detected with little smoothing. In the simulation, residual artifacts after perfect PMC were clearly visible (Fig. 2b). They can be largely corrected by the proposed correction scheme (Fig. 2h). It should be noted that, even without regularization, the best approximate solutions can still be achieved. This is likely due to the absence of noise. On the other hand, in experimental studies, regularization played an important role in optimizing the high intensity variations in regions where the magnetizations were perturbed by the strong field inhomogeneities. Moreover, it can prevent divergence of the solution at high iteration counts as demonstrated in Fig. 4c. The successful application, however, highly depends on proper selection of the regularization parameter (λ) that controls the degree of smoothness imposed on the reconstruction. In this study, the optimal λ was manually adjusted for subjective good image-quality. However, several quantitative methods for selection of λ such as the L-curve method [38], generalized cross-validation [39] and the discrepancy principle [40] may be useful to select the most appropriate λ for the proposed reconstruction. Moreover, the tridiagonal regularization matrix provided smoother solution [26] rather than using an identity. This is advantageous for the regions with high-intensity variation.

In the in vivo experiments, the largest B0 field change due to head movement during the acquisition was 250 Hz which caused 1.25 pixels shift for a readout BW of 200 Hz/pixel. This field change generated residual blurring artifact as illustrated in Figs. 7 and 8. However, this artifact is somewhat small. The images reconstructed by RSS and conventional CG-SENSE appeared slightly degraded, but still acceptable. This is due to the use of a small head coil (32-channel) that restricted movement. On the other hand, when using a larger head coil that allows greater motion, the artifacts may become a more relevant challenge as demonstrated in the phantom experiments. The proposed reconstruction may become more important to improve the image quality especially when scanning heads of children or uncooperative patients. In addition, correction of distortions due to B0 variation may be most important in sequences that are highly susceptible to field variations, such as multi-shot EPI, for which the correction may be more relevant even for smaller motion than in the examples in this study with a less sensitive FLASH acquisition. It is important to note that the proposed reconstruction requires an accurate field map. In this study, all acquired data had sufficiently high SNR and small ΔTE. As a result, artefact-free phase differences and field maps can be achieved via a fast and simple method (i.e., the Hermitian inner product, HP). However, Lu et al. [32] showed that the naive HP exhibits higher noise sensitivity than SENSE-based methods [41, 42]. In addition, using long TEs or high ΔTE may cause severely wrapped phase data that require phase unwrapping with more advanced but computationally expensive methods, e.g. UMPIRE [43].

In practice, several challenges require further investigation. First, the explicit determination of coil sensitivities for each motion pose is time consuming. However, it is fortunate that the coil sensitivity estimation does not require high resolution [13, 24, 25]. Thus, using a fast

pre-scan for acquiring low-res sensitivity maps prior to imaging [13, 35] may be possible. Second, although several techniques for dynamic characterization of the B_0 field [44, 45] have been developed, they require additional scan time and assume that the subject remains still for each measurement step. For stronger motion, the distortion caused by B_0 field inhomogeneity has been considered for single-shot EPI time series where each acquisition can provide a field map [19, 46]. Extension to multi-shot EPI and other spin-warp sequences is not obvious. Recently, there have been several efforts to predict field maps from air/tissue susceptibility distributions of the anatomy using magnetic field models [47, 48] which neither require additional scan time nor suffer from low SNR at air/tissue boundaries. Boegle et al. [49] showed that the quality of distortion correction using the model-based field maps in phantom experiments with arbitrary orientations is comparable to distortion correction based on measured field maps of the same object. The distortion-free PMC imaging of large moving object may be feasible if such corrections are employed. Even if the field maps can be determined for each motion pose, local signal dropouts cannot be recovered retrospectively. Such signal variations due to intra-voxel dephasing are likely the cause of residual artifacts in the corrected images (see Fig. 3b: the corrected images are geometrically correct but show significant signal loss around the air inclusion). Dynamic shimming may be able to address this aspect in part. Recently, Ward et al. [50] introduced real-time auto shimming by means of a navigator pulse sequence (shim NAV) to acquire field information for first order shim-compensated EPI acquisition in the presence of subject motion. A 3D EPI navigator [51] was also employed to achieve simultaneous motion and shim correction in single voxel MR spectroscopy. Keating et al. [52] showed that fast B0 mapping for an MRS voxel ($20 \times 20 \times 1.17$ mm^3) can be performed in approximately 120 ms. Moreover, field map free dynamic shimming [53] using a larger number of field map templates together with non-linear registration methods can produce a homogeneous field without acquisition time penalty. Knowing the higher than first order dynamic field fluctuations around the head may be helpful. These fluctuations can be monitored by field cameras [54] concurrently with image acquisition. Feedback of these global field changes into the high order shim coils [55] or reconstruction [56] may allow minimizing the field fluctuation-induced artifacts in motion correction. Finally, the proposed reconstruction is much more time consuming than traditional Fourier reconstruction due to the separation of data into several pipelines and iterative calculation. The applications of parallel computing by graphics processing units (GPUs) [57], and coil compression techniques [58] that reduce the data from many channels into fewer virtual coils may be ideally suited to improve the reconstruction speed.

Conclusion

This study demonstrates that geometric distortions due to gradient field nonlinearity as well as B0 field inhomogeneities can induce residual artifacts even in perfectly prospectively motion-corrected data especially in off-center and high susceptibility regions. These artifacts can be alleviated by the proposed technique that extends augmented SENSE by ΔB_0&GNL corrections.

Acknowledgments

The study was supported by the BMBF (Forschungscampus *STIMULATE*, 03FO16101A) and NIH (DA021146). We greatly appreciate all support from the BMMR Mo-Co team. C. Luengviriya thanks the Center for Advanced Studies of Industrial Technology, Kasetsart University for financial support.

References

1. Bydder M, Larkman DJ, Hajnal JV. Detection and elimination of motion artifacts by regeneration of k-space. Magn Reson Med. 2002; 47:677–686. [PubMed: 11948728]
2. Atkinson D, Hill DL, Stoyle PN, Summers PE, Clare S, Bowtell R, Keevil SF. Automatic compensation of motion artifacts in MRI. Magn Reson Med. 1999; 41:163–170. [PubMed: 10025625]
3. Batchelor PG, Atkinson D, Irarrazaval P, Hill DL, Hajnal J, Larkman D. Matrix description of general motion correction applied to multishot images. Magn Reson Med. 2005; 54:1273–1280. [PubMed: 16155887]
4. Thesen S, Heid O, Mueller E, Schad LR. Prospective acquisition correction for head motion with image-based tracking for real-time fMRI. Magn Reson Med. 2000; 44:457–465. [PubMed: 10975899]
5. Ward HA, Riederer SJ, Grimm RC, Ehman RL, Felmlee JP, Jack CR Jr. Prospective multiaxial motion correction for fMRI. Magn Reson Med. 2000; 43:459–469. [PubMed: 10725890]
6. Zaitsev M, Dold C, Sakas G, Hennig J, Speck O. Magnetic resonance imaging of freely moving objects: prospective real-time motion correction using an external optical motion tracking system. NeuroImage. 2006; 31:1038–1050. [PubMed: 16600642]
7. Maclaren J, Herbst M, Speck O, Zaitsev M. Prospective motion correction in brain imaging: a review. Magn Reson Med. 2013; 69:621–636. [PubMed: 22570274]
8. Maclaren J, Lee KJ, Luengviriya C, Speck O, Zaitsev M. Combined prospective and retrospective motion correction to relax navigator requirements. Magn Reson Med. 2011; 65:1724–1732. [PubMed: 21590805]
9. Banerjee S, Beatty PJ, Zhang JZ, Shankaranarayanan A. Parallel and partial Fourier imaging with prospective motion correction. Magn Reson Med. 2004; 69:421–433. [PubMed: 22488750]
10. Atkinson D, Larkman DJ, Batchelor PG, Hill DL, Hajnal JV. Coil-based artifact reduction. Magn Reson Med. 2004; 52:825–830. [PubMed: 15389945]
11. Aksoy, M. International Society for Magnetic Resonance in Medicine. Toronto: 2008. Effect of Motion-Induced Altered Coil Sensitivity on Parallel Imaging Performance. In: Proceedings of the 16th scientific meeting; p. 3111
12. Luengviriya, C. Proceedings of the ISMRM Workshop on Current Concepts of Motion Correction for MRI & MRM. Austria: 2010. Necessity of sensitivity profile correction in retrospective motion correction at 7T MRI.; p. 10
13. Bammer R, Aksoy M, Liu C. Augmented generalized SENSE reconstruction to correct for rigid body motion. Magn Reson Med. 2007; 57:90–102. [PubMed: 17191225]
14. Polzin JA, Kruger DG, Gurr DH, Brittain JH, Riederer SJ. Correction for gradient nonlinearity in continuously moving table MR imaging. Magn Reson Med. 2004; 52:181–187. [PubMed: 15236384]
15. Hu HH, Madhuranthakam AJ, Kruger DG, Glockner JF, Riederer SJ. Continuously moving table MRI with SENSE: application in peripheral contrast enhanced MR angiography. Magn Reson Med. 2005; 54:1025–1031. [PubMed: 16149061]
16. Yarach U, Luengviriya C, Danishad A, Stucht D, Godenschweger F, Schulze P, Speck O. Correction of gradient nonlinearity artifacts in prospective motion correction for 7T MRI. Magn Reson Med. 2015; 73:1562–1569. [PubMed: 24798889]
17. Jezzard P, Balaban RS. Correction for geometric distortion in echo planar images from B0 field variations. Magn Reson Med. 1995; 34:65–73. [PubMed: 7674900]
18. Jezzard P, Clare S. Sources of distortion in functional MRI data. Hum Brain Mapp. 1999; 8:80–85. [PubMed: 10524596]

19. Ooi MB, Muraskin J, Zou X, Thomas WJ, Krueger S, Aksoy M, Bammer R, Brown TR. Combined prospective and retrospective correction to reduce motion-induced image mis-alignment and geometric distortions in EPI. Magn Reson Med. 2013; 69:803–811. [PubMed: 22499027]
20. Speck O, Stadler J, Zaitsev M. High resolution single-shot EPI at 7T. Magn Reson Mater Phy. 2008; 21:73–86.
21. Sulikowska, A.; Wharton, S.; Glover, PM.; Gowland, PA. [12 August 2015] Will field shifts due to head rotation compromise motion correction.. ISMRM-ESMRMB in Milan. 2014. http://cds.ismrm.org/protected/14 MPresentations/0885/.
22. Fessler J, Sutton B. Nonuniform fast Fourier transforms using min–max interpolation. IEEE Trans Signal. 2003; 51:560–574.
23. Tao S, Trzasko JD, Shu Y, Huston J III, Bernstein MA. Integrated image reconstruction and gradient nonlinearity correction. Magn Reson Med. 2015; 74:1019–1031. [PubMed: 25298258]
24. Pruessmann KP, Weiger M, Bornert P, Boesiger P. Advances in sensitivity encoding with arbitrary k-space trajectories. Magn Reson Med. 2001; 46:638–651. [PubMed: 11590639]
25. Qu P, Luo J, Zhang B, Wang J, Shen GX. An Improved iterative SENSE reconstruction method. Magn Reson Eng. 2007; 31:44–50.
26. Hansen, PC. Rank-deficient and discrete ill-posed problems: numerical aspects of linear inversion. SIAM; Philadelphia: 1998. p. 247
27. Knoll F, Schultz G, Bredies K, Gallichan D, Zaitsev M, Hennig J, Stollberger R. Reconstruction of undersampled radial PatLoc imaging using total generalized variation. Magn Reson Med. 2013; 70:40–52. [PubMed: 22847824]
28. Fessler, J. The University of Michigan. Ann Arbor, Michigan, USA: 2014. Image reconstruction toolbox.. http://web.eecs.umich.edu/_fessler/irt/fessler.tgz. [12 April 2014]
29. Yoder DA, Zhao Y, Paschal CB, Fitzpatrick JM. MRI simulator with object-specific field map calculations. Magn Reson Imaging. 2004; 22:315–328. [PubMed: 15062927]
30. Maclaren J, Armstrong BSR, Barrows RT, et al. Measurement and correction of microscopic head motion during magnetic resonance imaging of the brain. PLoS ONE. 2012 doi:10.1371/journal.pone.0048088.
31. Wey, HY.; Huang, JC.; Hsu, YY.; Lim, K.; Kuan, WC.; Chen, CC.; Liu, HL. Proceedings of the 48th scientific meeting. The American Association of Physicists in Medicine (AAPM); Orlando: 2006. Image quality testing using an oil-filled ACR MRI phantom at 3.0 T.; p. 5044
32. Lu K, Liu TT, Bydder M. Optimal phase difference reconstruction: comparison of two methods. Magn Reson Imaging. 2008; 26:142–145. [PubMed: 17572035]
33. FMRIB Software Library, University of Oxford. [12 April 2015] 2012. http://www.fmrib.ox.ac.uk/fsl.
34. Robinson S, Jovicich J. B0 mapping with multi-channel RF coils at high field. Magn Reson Med. 2011; 66:976–988. [PubMed: 21608027]
35. Haase A, Frahm J, Matthaei D, Hanicke W, Merboldt KD. FLASH imaging. Rapid NMR imaging using low flip-angle pulses. J Magn Reson. 1986; 67:258–266.
36. Archip N, Clatz O, Whalen S, Dimaio SP, Black PM, Jolesz FA, Golby A, Warfield SK. Compensation of geometrical distortion effects on intraoperative magnetic resonance imaging for enhanced visualization in image-guided neurosurgery. Neurosurgery. 2008; 62:209–216. [PubMed: 18424988]
37. Sumanaweera T, Adler JR, Napel S, Glover GH. Characterization of spatial distortion in magnetic resonance imaging and its implications for stereotaxic surgery. Neurosurgery. 1994; 35:696–704. [PubMed: 7808613]
38. Vogel CR. Non-convergence of the L-curve regularization parameter selection method. Inverse Prob. 1996; 12(4):535–547.
39. Golub GH, Heath M, Wahba G. Generalized cross-validation as a method for choosing a good ridge parameter. Techno-metrics. 1979; 21(2):215–223.
40. Galatsanos NP, Katsaggelos AK. Methods for choosing the regularization parameter and estimating the noise variance in image restoration and their relation. IEEE Trans Image Process. 1992; 1(3):322–336. [PubMed: 18296166]

41. Walsh DO, Gmitro AF, Marcellin MW. Adaptive reconstruction of phased array MR imagery. Magn Reson Med. 2000; 43(5):682–690. [PubMed: 10800033]
42. Bernstein MA, Grgic M, Brosnan TJ, Pelc NJ. Reconstruction of phase contrast, phase array multicoil data. Magn Reson Med. 1994; 32:330–334. [PubMed: 7984065]
43. Robinson S, Horst S, Siegfried T. A method for unwrapping highly wrapped multi-echo phase images at very high field: UMPIRE. Magn Reson Med. 2014; 72:80–92. [PubMed: 23901001]
44. Hutton C, Bork A, Josephs O, Ceichmann R, Ashburner J, Turner R. Image distortion correction in fMRI: a quantitative evaluation. Neuroimage. 2002; 16(1):217–240. [PubMed: 11969330]
45. In MH, Speck O. Highly accelerated PSF-mapping for EPI distortion correction with improved fidelity. MAGMA. 2012; 25(3):183–192. [PubMed: 21814756]
46. Ooi MB, Krueger S, Muraskin J, Thomas WJ, Brown TR. Echo-planar imaging with prospective slice-by-slice motion correction using active markers. Magn Reson Med. 2011; 66(1):73–78. [PubMed: 21695720]
47. Koch KM, Papademetris X, Rothman D, de Graaf RA. Rapid calculations of susceptibility-induced magnetostatic field perturbations for in vivo magnetic resonance. Phys Med Biol. 2006; 51:6381–6402. [PubMed: 17148824]
48. Jenkinson M, Wilson JL, Jezzard P. Perturbation method for magnetic field calculations of nonconductive objects. Magn Reson Med. 2004; 52:471–477. [PubMed: 15334564]
49. Boegle R, Maclaren J, Zaitsev M. Combining prospective motion correction and distortion correction for EPI: towards a comprehensive correction of motion and susceptibility-induced artifacts. Magn Reson Mater Phy. 2010; 23:263–273.
50. Ward HA, Riederer SJ, Jack CR. Real-time auto shimming for echo planar timecourse imaging. Magn Reson Med. 2002; 48:771–780. [PubMed: 12417991]
51. Hess AT, Dylan Tisdall M, Andronesi OC, Meintjes EM, van der Kouwe AJW. Real-time motion and B0 corrected single voxel spectroscopy using volumetric navigators. Magn Reson Med. 2011; 66(2):314–323. [PubMed: 21381101]
52. Keating B, Ernst T. Real-time dynamic frequency and shim correction for single-voxel MR spectroscopy. Magn Reson Med. 2012; 68(5):1339–1345. [PubMed: 22851160]
53. Shi, Y.; Vannesjo, J.; Miller, K.; Clare, S. Proceedings of the 23rd scientific meeting. International Society for Magnetic Resonance in Medicine; Toronto: 2015. Field-Map-Free First-Order Dynamic Shimming.; p. 0096
54. Barmet C, De Zanche N, Pruessmann KP. Spatiotemporal magnetic field monitoring for MR. Magn Reson Med. 2008; 60:187–197. [PubMed: 18581361]
55. Duerst Y, Wilm BJ, Dietrich BE, Vannesjo SJ, Barmet C, Schmid T, Brunner DO, Pruessmann KP. Real-time feedback for spatiotemporal field stabilization in MR systems. Magn Reson Med. 2014; 73(2):884–893. [PubMed: 24634192]
56. Wilm BJ, Barmet C, Pavan M, Pruessmann KP. Higher order reconstruction for MRI in the presence of spatiotemporal field perturbations. Magn Reson Med. 2011; 65:1690–1701. [PubMed: 21520269]
57. Hansen MS, Atkinson D, Sorensen TS. Cartesian SENSE and k-t SENSE reconstruction using commodity graphics hardware. Magn Reson Med. 2008; 59(3):463–468. [PubMed: 18306398]
58. Zhang T, Pauly JM, Vasanawala SS, Lustig M. Coil compression for accelerated imaging with cartesian sampling. Magn Reson Med. 2013; 69:571–582. [PubMed: 22488589]

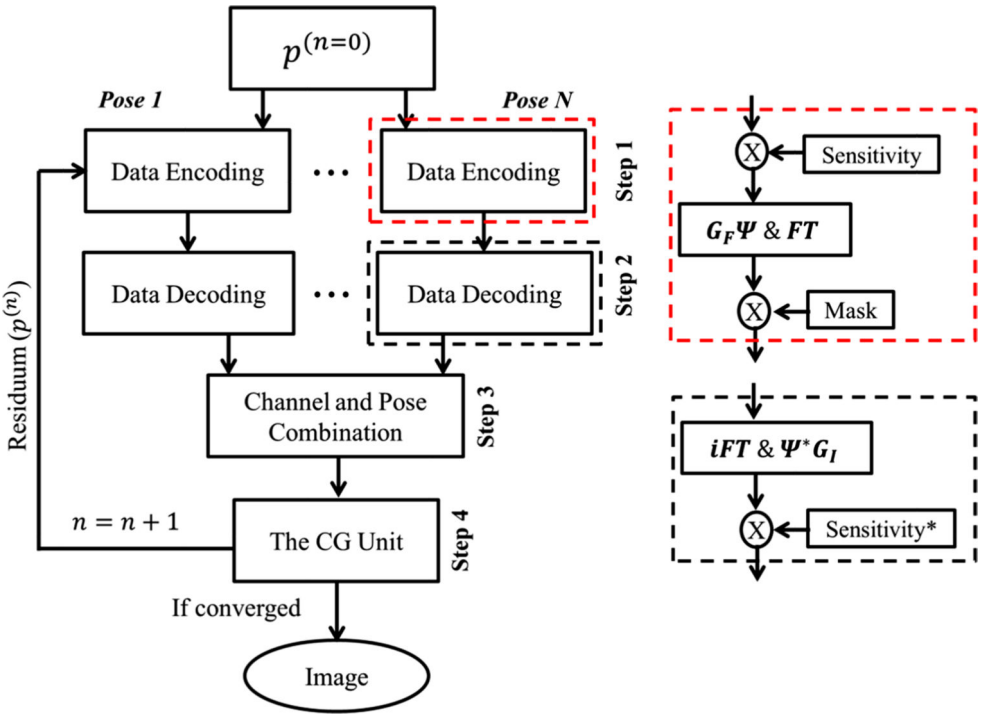

Fig. 1.

Schematic diagram of the augmented CG-SENSE with integrated ΔB_0&*GNL* corrections. The main diagram of the four steps in each iteration is shown on the *left*. The *right diagram* the implementation details of the data encoding (*red dashed box*) and the data decoding (*black dashed box*). The notation *asterisk* denotes complex conjugate

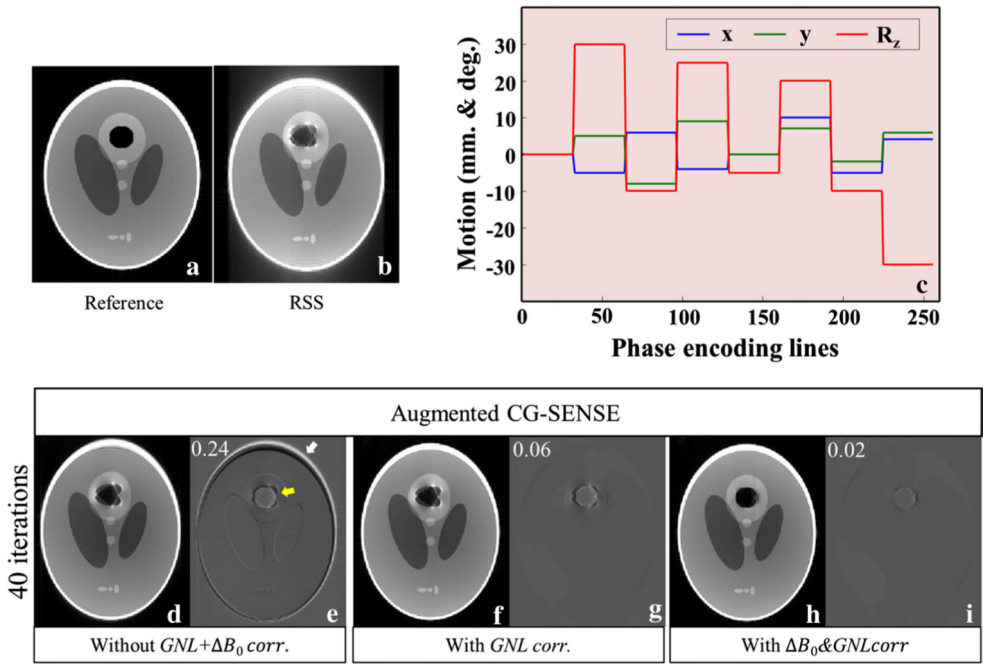

Fig. 2.

The reference (**a**), root-sum-of-squares (**b**), and corrected (**d**, **f**, **h**) images are identically windowed. Three parameters of 2D motion, shifted in *x* and *y* directions, rotated around *z*-axis with R_Z were assumed (**c**). The corrected images were reconstructed by the augmented CG-SENSE (**d**), with integrated *GNL* correction (**f**), and with integrated $GNL\&\Delta B_0$ corrections (**h**). The image differences (**e**, **g**, **i**) are the subtraction between each corrected image and reference. The RMSEs were superimposed on the upper left of the subtraction images

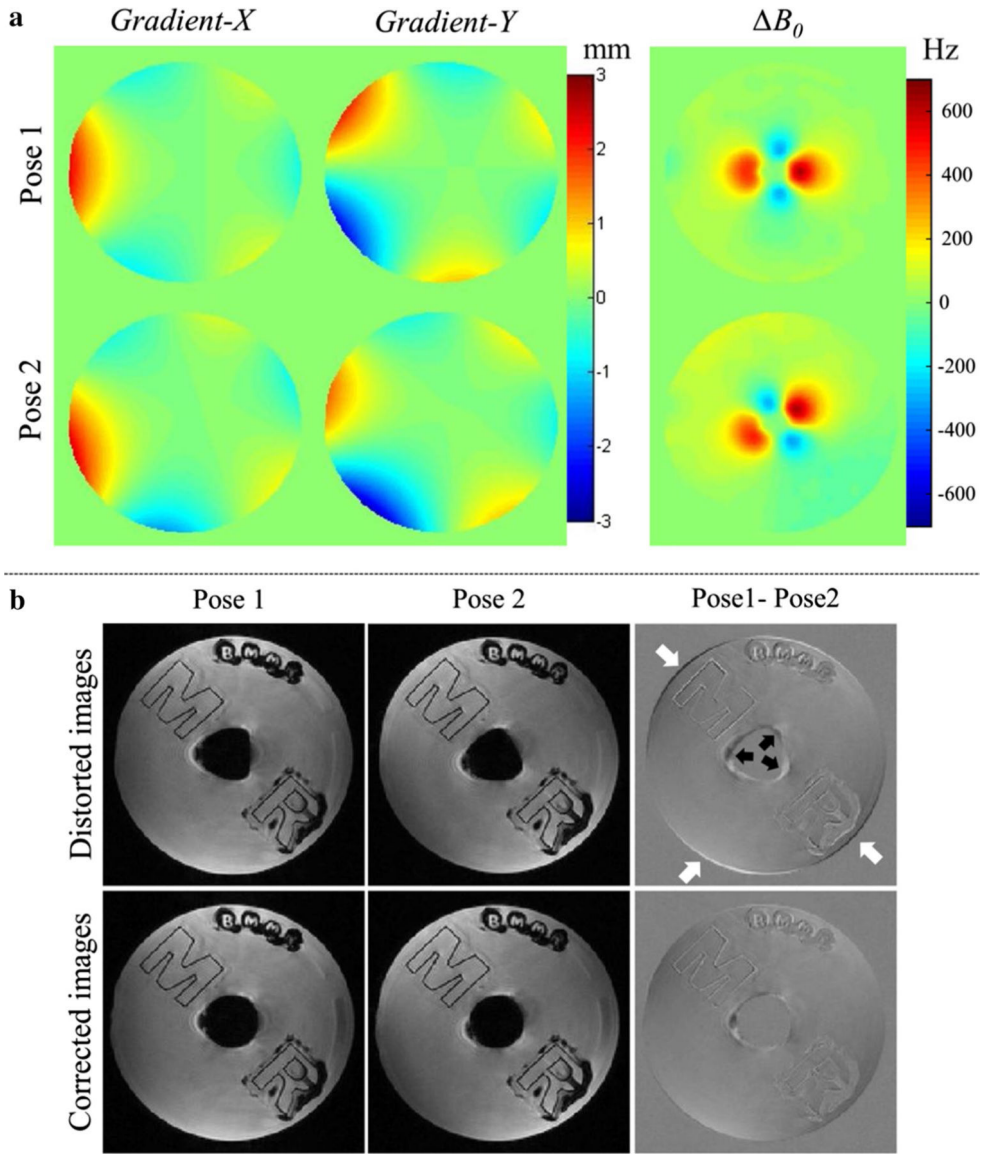

Fig. 3.

a The displacements of imaging gradients and B_0 field maps corresponding to pose1 and pose2. **b** *Upper row* The images at different poses were acquired with PMC enabled leading to identical orientations despite large object motion, but still show distortions due to *GNL* and ΔB_0. **b** *Bottom row* The image quality can be improved after *GNL* and ΔB_0 correction

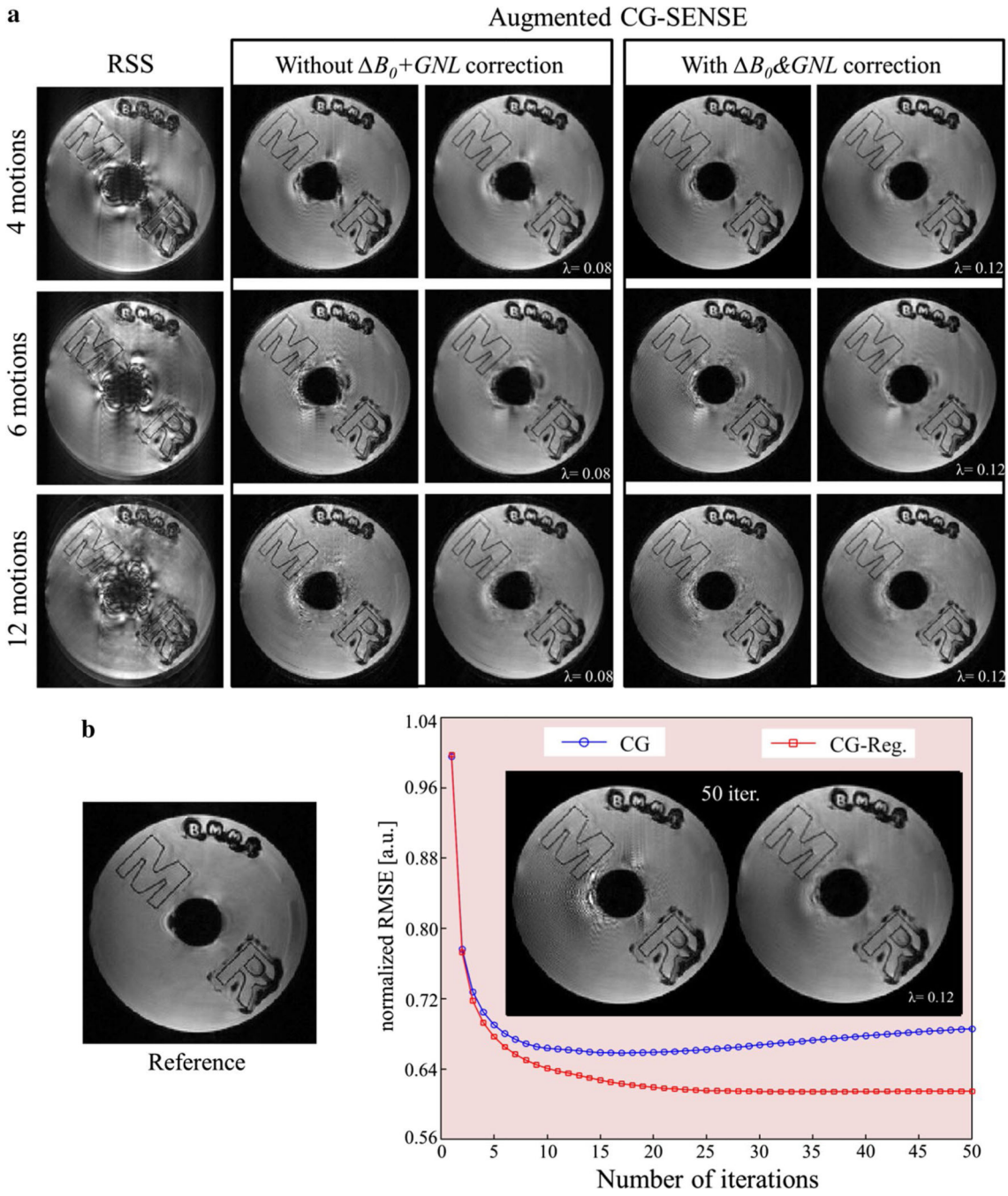

Fig. 4.

a All images are identically windowed; *1st column* root-sum-square images; *2nd* and *3rd columns:* images reconstructed by 20 iterations of augmented CG-SENSE without and with regularization, respectively; *4th* and *5th columns* images reconstructed by 20 iterations of augmented CG-SENSE with integrated ΔB_0&*GNL* corrections without and with regularization, respectively. **b** The regularization can stabilize the solution for high iteration counts. Note that the stationary pose1 image with ΔB_0&*GNL* corrections was the reference in calculating RMSE

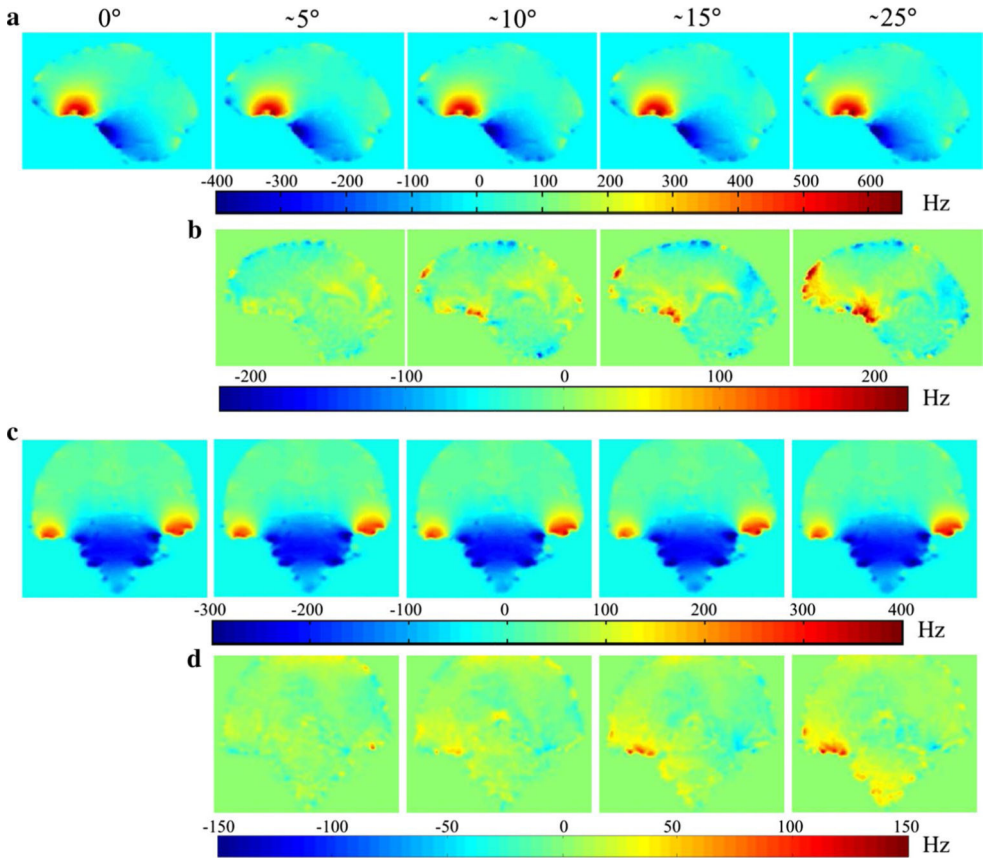

Fig. 5.

The susceptibility effects on the B0 field in the brain during motion. The field map information acquired at five different constant poses (0°, 5°, 10°, 15°, and 25° around *z*-axis of the scanner). **a**, **c** The B_0 field maps for the frontal lobes (*sagittal plane*) and the temporal lobes (*coronal plane*), respectively. **b**, **d** The field differences between each field map and the field map obtained in the 0° reference position

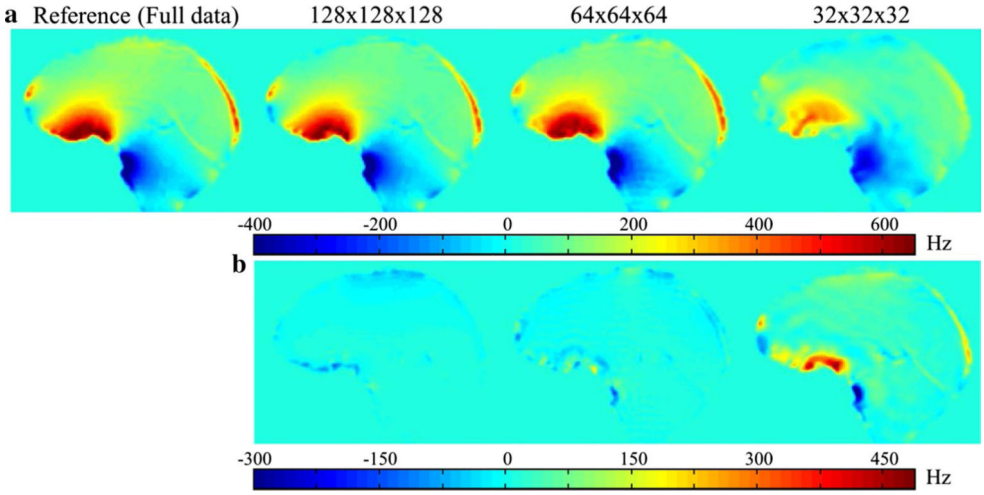

Fig. 6.

a The B0 field maps at the frontal region of the brain reconstructed at different resolutions from the same *k*-space data. **b** The field differences between each field map and the field map obtained from full *k*-space data

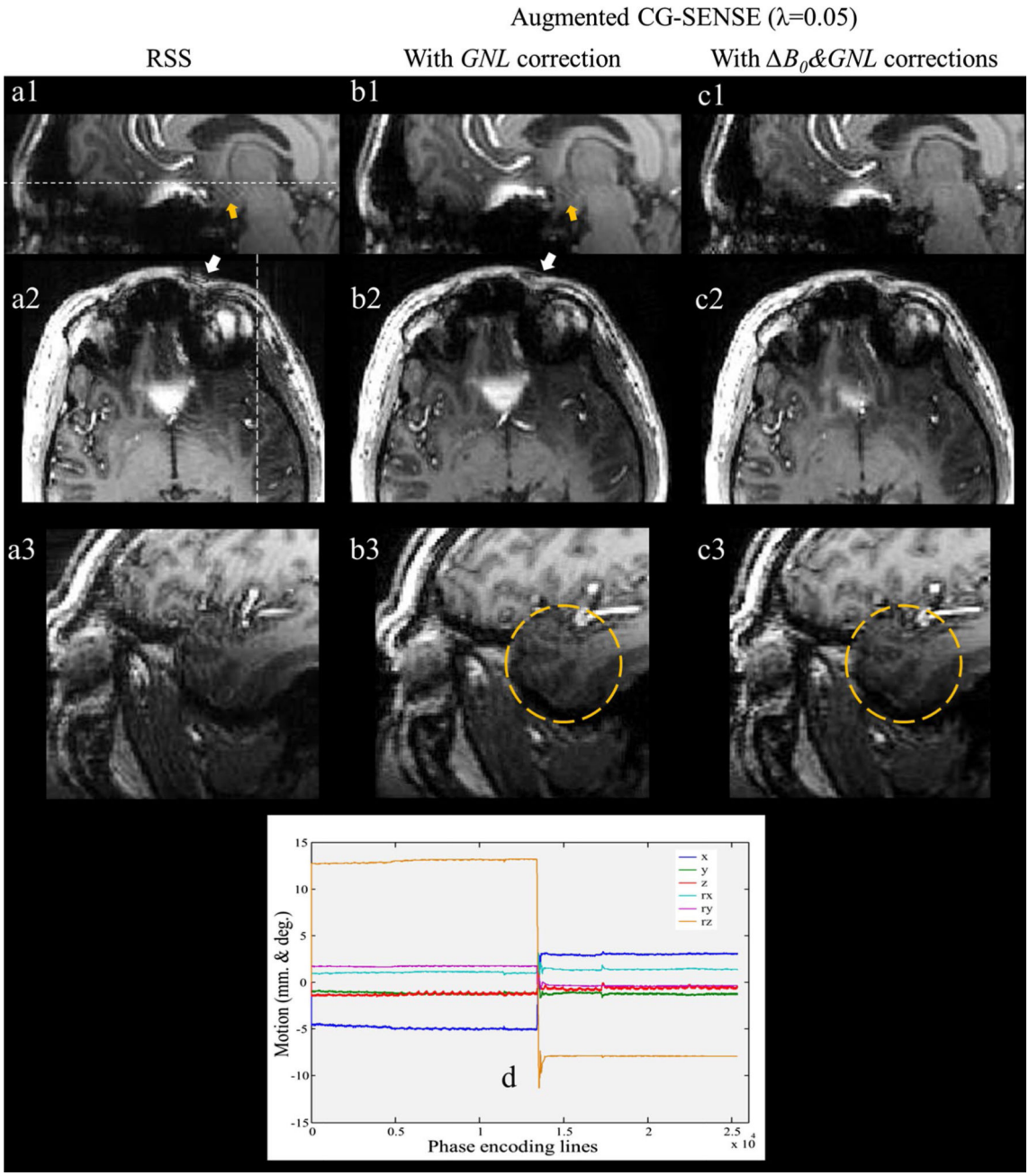

Fig. 7.

1st column (**a1**–**a3**) root-sum-of-squares images of the prospectively motion-corrected acquisition. 2nd column (**b1**–**b3**) images after five iterations of augmented CG-SENSE with integrated *GNL*. 3rd column (**c1**–**c3**) images with integrated ΔB_0&*GNL*. The axial images in the 2nd row and the sagittal images in the 3rd row correspond to the *white lines* in images **a1** and **a2**, respectively. The *yellow circles* in b3 and c3 *highlight* the artifact from ΔB_0 and the image improvement, respectively. **d** Six parameters of 3D motion from tracking log file (*x*, *y*, *z* shifts and R_x, R_y, R_z rotations)

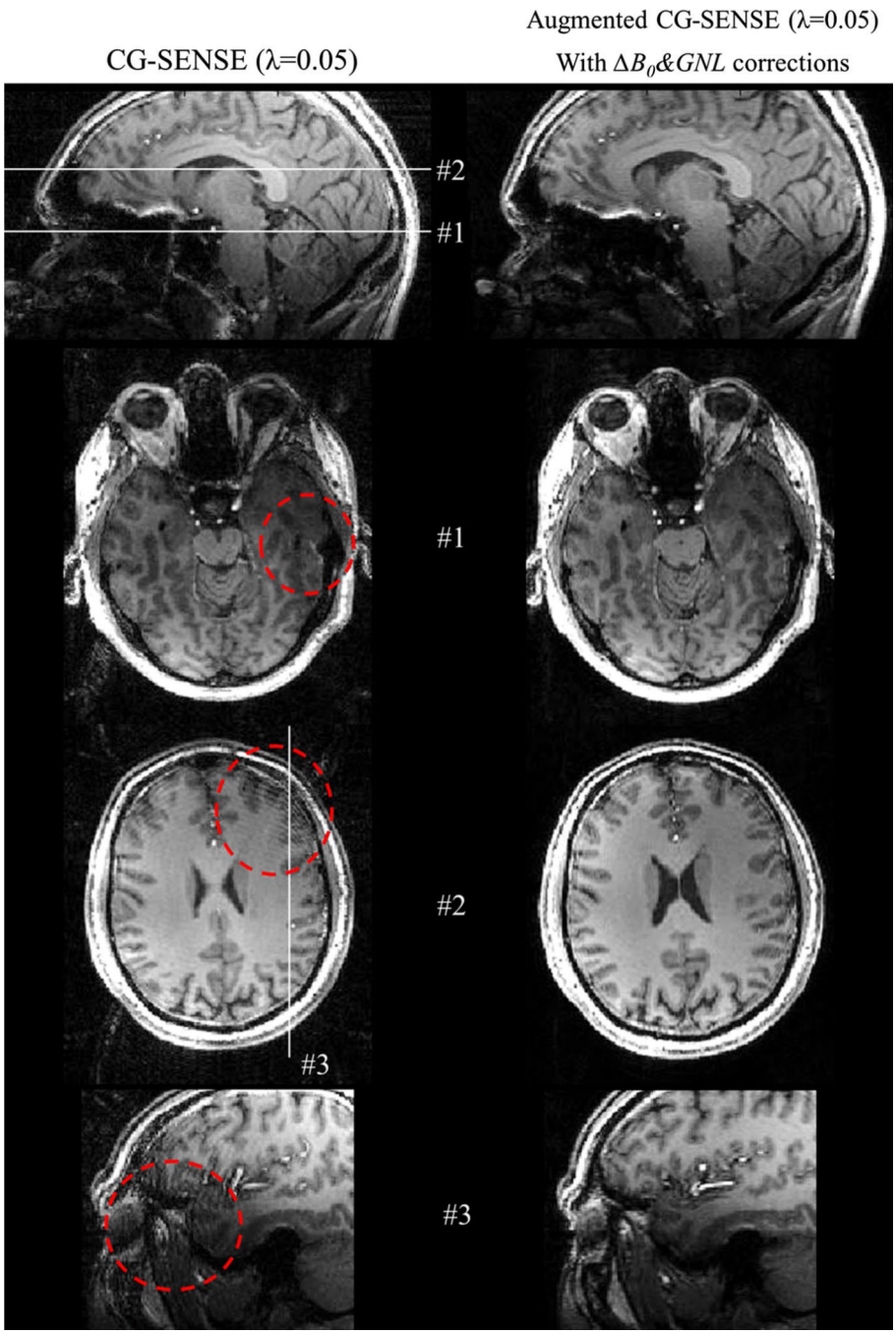

Fig. 8.

The 2 × 2 undersampled *k*-space data reconstructed by the CG-SENSE and the augmented CG-SENSE with integrated ΔB_0&*GNL*. The axial images in the *2nd and 3rd rows* correspond to the white *lines #1* and *#2*, respectively. The sagittal images in the *4th row* correspond to the *white lines #3*